

Operando XAS Study of Pt-Doped CeO₂ for the Nonoxidative Conversion of Methane

Daniel Eggart,[†] Xin Huang,[†] Anna Zimina, Jiuzhong Yang, Yang Pan, Xiulian Pan,* and Jan-Dierk Grunwaldt*



Cite This: *ACS Catal.* 2022, 12, 3897–3908



Read Online

ACCESS |



Metrics & More



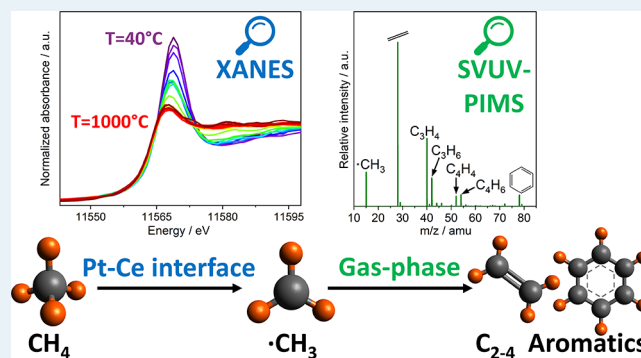
Article Recommendations



Supporting Information

ABSTRACT: The methane to olefins, aromatics, and hydrogen (MTOAH) process via Pt/CeO₂ catalysts poses an attractive route to improve yield and stability for the direct catalytic conversion of methane. In this study, two sets of samples, one composed of PtO_x single sites on ceria and the other with additional Pt agglomerates, were prepared. Both sets of samples showed enhanced catalytic activity for the direct conversion of methane exceeding the performance of pure ceria. Pulsed reaction studies unraveled three reaction stages: reduction of the ceria support during activation, an induction phase with increasing product formation, and finally, stable running of the catalytic reactions. The reduction of ceria was confirmed by X-ray absorption spectroscopy (XAS) after conducting the MTOAH reaction. *Operando* X-ray absorption spectroscopy at challenging reaction temperatures of up to 975 °C in combination with theoretical simulations further evidenced an increased Pt–Ce interaction upon reaction with CH₄. Analysis of the extended X-ray absorption fine structure (EXAFS) spectra proved decoration and encapsulation of the Pt particles by the CeO₂/Ce₂O₃ support or a partial Ce–Pt alloy formation due to the strong metal–support interaction that developed under reaction conditions. Moreover, methyl radicals were detected as reaction intermediates indicating a reaction pathway through the gas-phase coupling of methyl radicals. The results indicate that apart from single-atom Pt sites reported in the literature, the observed Pt–Ce interface may have eased the activation of CH₄ by forming methyl radicals and suppressed coke formation, significantly improving the catalytic performance of the ceria-based catalysts in general.

KEYWORDS: platinum, ceria, SMSI, direct methane conversion, operando XAS



1. INTRODUCTION

With declining crude oil resources, natural gas is attracting increasing attention as a substitute in the energy sector and for chemical feedstocks. Recently discovered unconventional gas reserves, such as shale gas or coalbed methane, are mostly located in scarcely populated areas. As long-distance transportation of methane is often economically unviable, on-site conversion of methane to liquid value-added chemicals is a promising approach. In contrast to traditional multistep processes via synthesis gas and subsequent methanol or Fischer–Tropsch synthesis, the direct conversion of methane (DCM) route potentially allows higher efficiency in energy-saving and carbon-atom utilization.^{1,2} DCM can be realized by oxidative coupling of methane (OCM)³ or nonoxidative methane dehydrogenation (MDA)⁴ to olefins and aromatics. Since Keller and Bhasin introduced OCM,³ a variety of catalysts have been tested. However, the industrial application is still limited by low C₂ hydrocarbons yields (<25%) for most of the catalysts due to overoxidation leading to CO and CO₂ byproducts.¹ Zeolite-based molybdenum catalysts are very attractive for MDA but showed some severe deactivation due

to coke build-up.⁵ The current research focused on new approaches and concepts to overcome these low yield and stability issues.¹ Guo et al.⁶ have recently reported an iron single-site catalyst with outstanding performance for the direct conversion of methane under nonoxidative conditions at reaction temperatures above 950 °C. At such high reaction temperatures, the formation of methyl radicals followed by coupling to thermostable products such as ethylene, benzene, and hydrogen was reported.⁶ A long-term stable methane to olefins, aromatics, and hydrogen (MTOAH) reaction was observed, probably because the coke formation on the surface of the catalyst was suppressed by the absence of large metal iron nanoparticles.^{7,8} Likewise, Xie et al.⁹ found platinum single sites embedded on CeO₂ nanoslabs (fluorite phase) to convert

Received: January 6, 2022

Revised: February 25, 2022

methane into mainly C₂ hydrocarbons at 900 °C. However, platinum nanoparticles of 3–4 nm size on ceria showed significantly lower catalytic performance with much higher coke selectivity.⁹ Wen et al.¹⁰ performed theoretical calculations for DCM on Pt-atom-substituted Ce on a CeO₂(111) surface and concluded that single Pt atoms were more resistant against carbon deposition and favored higher ethylene selectivity than Pt clusters of 3 and 10 atoms. Bajec et al.¹¹ showed that a 0.1% Pt/CeO₂ single-atom catalyst started converting CH₄ at 780 °C. The proposed microkinetic model suggests the conversion of CH₄ on Pt single sites with CH₄ adsorption, the abstraction of the first •H radical from its neutral CH₄ molecule, and the desorption of H₂ as the most important reaction steps. Pt single atoms and ensembles on CeO₂ were also found to be highly active for other catalytic reactions, such as CO oxidation, selective CO₂ reduction, and the three-way catalytic reaction in which CO and C₃H₆ are oxidized and NO is simultaneously reduced.¹² However, *operando* studies have shown that Pt clusters may form and thus serve as the active species. Maurer et al.¹³ showed, *e.g.*, that Pt reversibly disperses on the ceria surface above 600 °C and thereby even restructures the support. The Pt single sites are typically bonded to square-planar hollow positions of the ceria support. Kottwitz et al.¹⁴ further refined that Pt²⁺ single sites bind to the hollow sites of perturbed (100) CeO₂ surface planes and thereby induce substantial strain within the support lattice in the vicinity to the Pt atom. Stadnichenko et al.¹⁵ reported a reduction of PtO₂ nanoparticles (<1 nm) on CeO₂ in vacuum starting at 250 °C occurring stepwise from Pt⁴⁺ over Pt²⁺ to Pt⁰. Generally, Pt single sites were shown to be stable in an oxidative atmosphere (air) at up to 800 °C,¹⁶ whereas sintering occurred in the reductive atmosphere (H₂) at 150 °C.¹⁷

Since doping of Pt over CeO₂ has been shown to lower the CH₄ activation barrier,¹⁸ synergetic effects of Pt and CeO₂ may also play a role in the activation of CH₄.⁹ Tauster et al.¹⁹ proposed that noble metals supported on TiO₂ experience a strong metal–support interaction (SMSI) when reduced in H₂. Meriaudeau et al.²⁰ suggested that for the H₂/CO reaction over Pt/CeO₂, an enhanced methanol formation might be explained by a Ce–Pt alloy formation. Bernal et al.²¹ showed for 4% Pt/CeO₂ that two-thirds of the Pt crystallites are encapsulated by ceria after H₂ reduction at 700 °C and CePt₅ particles form at 900 °C, whereas the deactivation of the catalyst is concluded to be caused by an increased support reduction and not by encapsulation or alloying. To design efficient, highly active, and stable catalysts for the direct conversion of methane, an analysis of the local Pt environment on CeO₂ during the reaction is needed.

In the present study, we aim at understanding the evolution of the Pt/CeO₂ active sites and product formation pathways during nonoxidative methane conversion using *operando* studies. Two sets of samples were prepared and thoroughly characterized starting from atomically dispersed Pt on nanocrystalline ceria by flame spray pyrolysis and a combination of Pt aggregates with single sites by incipient wetness impregnation on a commercial ceria support for comparison. Pulsed reaction studies and *operando* X-ray absorption spectroscopy (XAS) measurements at up to 975 °C were conducted to shed light on the activation of the catalyst through increased Pt–Ce interaction of differently derived and thus differently structured Pt/CeO₂ samples. Finally, the gas-phase reaction intermediates and products were analyzed by synchrotron-based vacuum ultraviolet photoionization mass spectrometry (SVUV-PIMS).

2. EXPERIMENTAL SECTION

2.1. Sample Preparation. Ceria catalysts doped with 0.5 and 1.0 wt % Pt were prepared by flame spray pyrolysis (FSP, similar to ref 22) and incipient wetness impregnation (WI, similar to ref 23) and were calcined at 1000 °C in air to potentially generate single sites in both cases.¹³ The samples are denoted 0.5 Pt (FSP), 1.0 Pt (FSP), 0.5 Pt (WI), and 1.0 Pt (WI), respectively. In the case of FSP, precursor solutions were prepared by dissolving specified amounts of platinum(II) acetylacetonate (98%, abcr) and cerium(III) 2-ethylhexanoate 49% in 2-ethylhexanoic acid (12% Ce, Alfa Aesar) in xylene (VWR Chemicals). The concentration of the total metal precursor was 0.5 mol/L. The precursor solutions were fed through a capillary into a methane/oxygen flame (750 mL/min CH₄, 1600 mL/min O₂) at 5 mL/min using a syringe pump (World Precision Instruments) and were dispersed with oxygen (5 L/min). A cylindrical steel vessel with a glass fiber filter (24 cm diameter, Whatman GF6) was placed above the flame. The produced particles were collected on this filter with the aid of a vacuum pump with an established setup at the Institute for Chemical Technology and Polymer Chemistry (ITCP) at KIT analogously to the apparatus described in the literature.²⁴

The WI procedure was performed by a robot-controlled preparation unit (Accelerator SLT106 Parallel Synthesizer—SLT CATIMPREG, ChemSpeed Technologies).²⁵ Herein, commercial CeO₂ (Sigma Aldrich, 99.95%, Brunauer–Emmett–Teller (BET) surface area: 40 m²/g) was impregnated with an aqueous solution of tetraammineplatinum(II) nitrate (VWR, >99.9%) and then dried at 70 °C under reduced pressure.

2.2. Characterization. N₂ physisorption measurements according to the Brunauer–Emmett–Teller (BET) method were performed at –196 °C using a BELSOPRP Mini II analyzer (MicrotracBEL) to estimate the surface area and pore volume. The samples were degassed for 2 h at 300 °C prior to the measurement.

The samples before and after catalytic testing were examined in an FEI Titan 80-300 aberration-corrected electron microscope (TEM) operated at 300 kV at the Karlsruhe Nano Micro Facility (KNMF, KIT). The samples were prepared by depositing a small amount of sample in ethanol on a holey carbon-coated gold grid. The particle size distribution was estimated with the software package ImageJ²⁶ assuming an elliptical size of the Pt particles. High-angle annular dark-field scanning transmission electron microscopy (HAADF-STEM) measurements were carried out on a JEM ARM300F microscope operated at 200 kV.

Diffusive reflectance infrared Fourier transform spectroscopy (DRIFTS) was performed on a Bruker Vertex 70 instrument with a Hg–Cd–Te (MCT) detector using a Praying Mantis high-temperature reaction chamber with KBr windows. The cell temperature was controlled by two heating cartridges and a water cooling system inside the cell. The outlet gases were monitored using a Pfeiffer Vacuum OmniStar GSD 320 mass spectrometer (MS). About 150 mg of the sample was diluted to 5 wt % with CaF₂ (100–200 μm) and filled into the sample holder. Using a gas stream of 10 mL/min, the catalyst was heated under 20% O₂/Ar flow (gas composition is always given in vol %) to 350 °C for 30 min, and after cooling to 40 °C a background spectrum (30 scans, 4 cm^{–1} resolution) was recorded. Subsequently, the gas composition was switched to

5% CO/He for 40 min, and after purging with He for 30 min the spectra were recorded.

2.3. Catalytic Activity. The catalytic activity tests were conducted in a fixed-bed quartz tubular reactor with an internal diameter of 11 mm. A total of 300 mg powdered catalyst with a sieve fraction of 400–840 μm was packed resulting in a catalyst bed of 3 mm length. The Mears criterion for external mass transfer and the Weisz–Prater criterion for internal mass transfer were estimated, and the data showed that both external and internal mass transfer effects can be neglected (for further details, cf. Supporting Information). The catalyst bed was located in the middle of the constant temperature zone of about 100 mm, the temperature was regulated with a controller (Al-708P, Xiamen Yudian Automation Technology Co.), and the thermocouple was placed outside the reactor close to the middle of the catalyst bed. The sample was heated from room temperature to the operating temperature with a ramp rate of 7 $^{\circ}\text{C}/\text{min}$ in a pure Ar flow (100 mL/min). The preheater was kept at 750 $^{\circ}\text{C}$. After flushing with an Ar flow for 10 min, the reaction started by switching on the feed gas. In our study, the feed gas composition of 90% CH_4/N_2 (N_2 as an internal standard) and the reactant gas flow (11.7–14.1 L/(g·h) space velocity; 8.6–10.2 1/h weight hourly space velocity (WHSV)) was chosen as industrially more relevant conditions compared to previously reported studies (0.9–2.6 1/h WHSV for pure CH_4 gas flow;¹¹ 6 L/(g·h) space velocity of 1% CH_4/He ⁹). The effluents were analyzed with an online 7890B Agilent GC equipped with TCD (HayeSep Q column) and FID (HP-1 capillary column) detectors. Methane conversion, hydrocarbon product selectivity, and coke deposition selectivity were calculated according to the carbon balance.²⁷

To follow the catalyst activation period, pulsed reaction studies were conducted at conditions similar to the fixed-bed catalytic activity tests. A six-way valve equipped with a sample loop was used to pulse 5 mL of 90% CH_4/He every 6 min to the sample and 30 mL/min Ar was fed as a carrier gas. A sieve fraction of 400–840 μm of 300 mg of powdered catalyst was fixed in a quartz tubular reactor of 4 mm inner diameter resulting in a catalyst bed of 15 mm length. The sample was heated from room temperature to 975 $^{\circ}\text{C}$ with a ramp rate of 7 $^{\circ}\text{C}/\text{min}$ in a pure Ar flow (30 mL/min). The preheater was kept at 750 $^{\circ}\text{C}$. The effluents were monitored using an online mass spectrometer (Pfeiffer Vacuum, Omnistar GSD 320), and the following products with corresponding mass-to-charge-ratios (m/z) were recorded: H_2 (2), He (4), CH_4 (16), H_2O (18), $\text{C}_2\text{H}_4/\text{C}_2\text{H}_6$ (27), CO (28), CO_2 (44), and C_6H_6 (78).

2.4. Synchrotron-Based Vacuum Ultraviolet Photoionization Mass Spectrometry. Gaseous reaction components were detected by synchrotron-based vacuum ultraviolet photoionization mass spectrometry (SVUV-PIMS) at the combustion station of the National Synchrotron Radiation Laboratory (NSRL, Hefei, China).²⁸ Synchrotron radiation from an undulator beamline (BL03U) was monochromatized with a 200 lines/mm laminar grating covering the photon energy from 7.5 to 22 eV with an energy resolving power of 3000 ($E/\Delta E$ @ 10 eV).²⁹ Typically, 200 mg of the catalyst was loaded in a horizontal quartz reactor (O.D.: 10 mm, I.D.: 7 mm, L : 480 mm). The pressure within the catalytic reactor was maintained at 45 mbar by a closed-loop control connected to a pressure sensor, a butterfly valve, and a vacuum pump.³⁰ Each sample was first heated to 1000 $^{\circ}\text{C}$ in an Ar flow and after reaching the reaction temperature, the feed gas was switched to CH_4 at 12 L/(g·h). A small fraction of the product gas from the catalyst bed is

sampled through a quartz nozzle (I.D.: 450 μm) into the ionization chamber. Therein, the molecular beam is crossed by the synchrotron VUV light. The thereby ionized molecules are then mass-analyzed with a time-of-flight mass spectrometer (Agilent 6224). The relative mole fraction of the products is calculated according to ref 31 (for further details, cf. Supporting Information).

2.5. X-ray Absorption Spectroscopy. X-ray absorption spectra (XAS) in terms of the X-ray absorption near-edge structure (XANES) and extended X-ray absorption fine structure (EXAFS) at the Pt L_3 and Ce L_3 absorption edges were recorded at the P65 beamline of the PETRA III synchrotron radiation source (DESY, Hamburg) in a fluorescence mode using a 7 pixel HPGe detector (Canberra). X-rays were produced by means of an 11-period undulator, and higher harmonics were rejected by a pair of Rh-coated plane mirrors installed in front of the monochromator. The energy of X-ray photons was further selected by a Si(111) double-crystal monochromator and the beam size was set with slits to $1 \times 0.2 \text{ mm}^2$.³² CePt₅ (MaTeCK Material-Technologie & Kristalle GmbH) and PtO₂ (Sigma Aldrich) powder references were pressed into pellets with cellulose and measured *ex situ*. For *operando* investigations, typically about 20 mg of 100–200 μm catalyst sieve fraction was fixed in a quartz capillary microreactor (O.D.: 1.5 mm and wall thickness: 0.02 mm) between two quartz wool plugs to give a catalyst bed of 6 mm length and heated in a home-built high-temperature cell.³³ The reaction gases were dosed with MFCs (Bronkhorst) at a space velocity of 13 L/(g·h) similar to the catalytic tests. Exhaust gas lines were heated to 150 $^{\circ}\text{C}$, and product gases were analyzed by mass spectrometry (Pfeiffer Vacuum, OmniStar GSD 320). The samples were first heated in He to 975 $^{\circ}\text{C}$, cooled to 40 $^{\circ}\text{C}$ to measure EXAFS followed by a 1 h reaction at 975 $^{\circ}\text{C}$ in 90% CH_4/He . The whole *operando* XAS measurement procedure is shown in Figure S15. The spectra were normalized and background-subtracted using the ATHENA program from the IFFEFIT software package.³⁴ The k^2 - and k^3 -weighted EXAFS functions were Fourier-transformed in the k range of 2.5–10 \AA^{-1} and multiplied by a Hanning window with a sill size of 1 \AA^{-1} . The structure refinement was performed in R-space using ARTEMIS software (IFFEFIT)³⁴ with theoretical backscattering amplitudes and phase functions calculated by FEFF 6.0.25.³⁵ The theoretical data were fitted to the experimental spectra by a least-squares method in an R-space between 1 and 4 \AA^{-1} . The amplitude reduction factor ($S_0 = 0.80$) was derived using the reference spectrum of the Pt foil and the number of identical paths (CN), change in the half path length (ΔR), the energy discrepancy from theoretical values (ΔE_0), and the Debye–Waller factor (σ^2) were fitted for the Pt foil and CePt₅ reference spectra and refined with Pt,³⁶ PtO₂,³⁷ and Ce₃Pt₄³⁸ crystal structures from the literature.

XANES spectra at the Pt L_3 absorption edge of clusters generated from Pt,³⁶ CePt,³⁹ Ce₃Pt₄,³⁸ CePt₅,⁴⁰ Ce₇Pt₃,⁴¹ CePt₂,⁴⁰ and CePt₃⁴² experimental crystal structures were simulated using the computer code FEFF9 and were aligned to the measured Pt reference.⁴³ The polarization dependence, core–hole effects, and local field corrections were based on self-consistent, spherical muffin-tin scattering potentials. The Hedin–Lundqvist potential was chosen, and SCF (self-consistent field) and FMS (full multiple scattering) cutoff radii of 5 and 9 \AA , respectively, were employed (for further details, cf. Supporting Information).

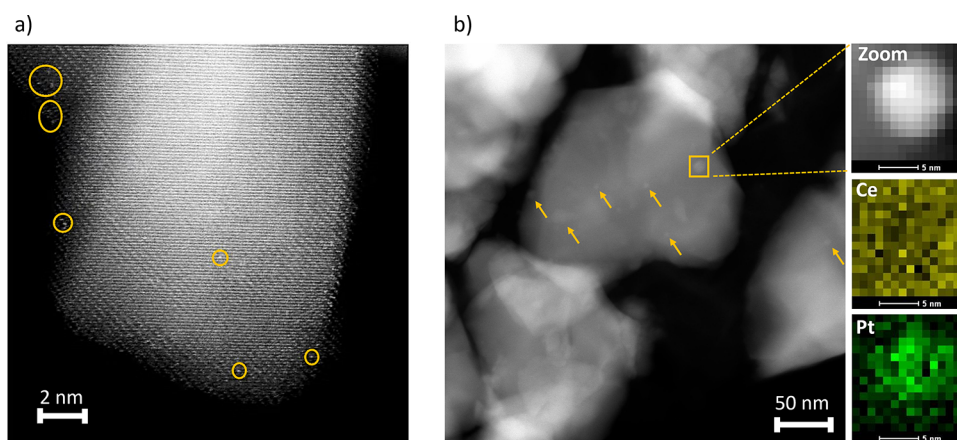


Figure 1. (a) HAADF-STEM image of the as-prepared 0.5 Pt (FSP)_{ap} with Pt single sites marked in circles. (b) STEM image of 0.5 Pt (FSP)_{spent} after catalytic testing; Pt particles are marked with orange arrows including a zoom on the orange box showing EDX maps of a Pt particle.

3. RESULTS AND DISCUSSION

3.1. Basic Sample Characterization. Two sets of catalysts with nominal 0.5 and 1 wt % Pt loadings on CeO₂ were prepared by the versatile flame spray pyrolysis (FSP) method to obtain Pt/CeO₂ in a one-step approach and by the robot-controlled reference process of incipient wetness impregnation (WI). The measured Pt loadings, which are close to the targeted loading, and BET surface areas are listed in Table S1. XRD measurements confirmed that all catalysts are composed of fluorite phase ceria. The samples exhibited surface areas in the range of about 20–40 m²/g and thereby allowed evaluating the effect of Pt dispersion and oxidation state on the catalytic activity. Only fresh 1 Pt (FSP) showed minor Pt reflections in the XRD indicating reduced Pt nanoparticles (Figure S1). The samples loaded with 0.5 wt % Pt were investigated in further detail.

The 0.5 wt % Pt fresh catalyst prepared by the FSP method (denoted 0.5 Pt (FSP)_{ap}) showed slabs of nanoceria in a range from 12 to 45 nm (TEM, Figure S3a) and revealed highly dispersed Pt single sites (HAADF-STEM, Figure 1a) with no apparent Pt nanoparticles. The as-prepared WI samples contain ceria particles with aggregated platinum in different sizes, probably due to the lower surface area that is half of that of the FSP sample (EDX maps on STEM images, Figure S3b). After catalytic testing, sintering to Pt nanoparticles was observed for 0.5 Pt (FSP) in Figure 1b and 0.5 Pt (WI) with mean diameters of 9 and 5 nm, respectively (denoted 0.5 Pt (FSP)_{spent} and 0.5 Pt (WI)_{spent}; for further STEM and HAADF-STEM images as well as particle size distributions, see Figures S4–S6 in the Supporting Information). However, metallic Pt reflections were not observed in the XRD measurements for the spent catalysts, likely due to rather low Pt loading.

In situ CO-DRIFTS studies were performed on fresh and spent catalysts. Both fresh samples with 0.5 wt % Pt loading revealed a distinct peak at about 2090 cm⁻¹ assigned to CO adsorbed on Pt single sites (Figure 2).^{13,44} The as-prepared 0.5 Pt (WI) sample showed a slightly lower intensity of the CO-adsorption band, compared to the FSP catalyst, probably due to the aggregated Pt resulting in a lower number of single-atom Pt sites.⁴⁵ Interestingly, CO-DRIFTS measurements of both spent samples exhibited no distinct adsorption peak for Pt single sites and no adsorption band from 2000 to 2200 cm⁻¹. This is most likely due to inaccessible Pt sites, hinting at encapsulation of the formed Pt nanoparticles by the ceria support or a Ce–Pt alloy formation (for further details, cf. the section on Discussion of the

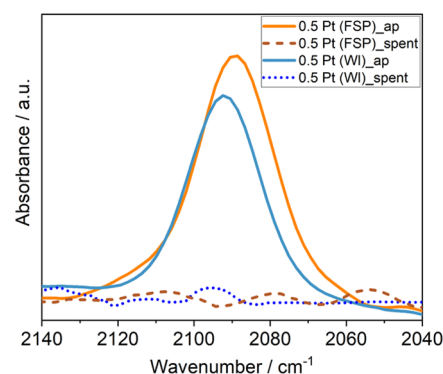


Figure 2. *In situ* CO-DRIFTS spectra for the fresh (_{ap}) and catalytically tested (_{spent}) 0.5 Pt (FSP) and 0.5 Pt (WI) samples in 5% CO/He at 40 °C (after flushing in He, CO-bands for the spent catalysts in the presence of CO are observed, see the supporting information, Figure S7).

XAS Studies). Dynamic evolution of the CO-DRIFT spectra during CO desorption for the spent catalysts is shown in Figure S7 (for further details, see the discussion in the Supporting Information). Raman spectroscopic results for the as-prepared samples suggest that Pt is anchored on the surface oxygen of ceria forming Pt–O–Ce bonds and that after reaction these cationic Pt species were reduced (Figure S8). H₂-TPR measurements showed distinct reduction peaks below 200 °C assigned to lattice oxygen in the vicinity of cationic Pt single sites (Pt–O–Ce bond) only for the as-prepared and not for the spent samples (Figure S9). For further details on Raman spectroscopy and H₂-TPR measurements, see the discussion in the Supporting Information. It can therefore be concluded that the single-atom Pt sites anchored on surface ceria through Pt–O–Ce bonds of the as-prepared catalysts sinter during methane conversion to form reduced Pt nanoparticles. However, the co-existence of very small amounts of Pt single sites cannot be ruled out.

3.2. Catalytic Performance. The catalytic activities of 0.5 and 1.0 wt % Pt on CeO₂ prepared via WI and FSP are shown in Figure 3. Note that a blank reactor was shown in a previous publication to exhibit a rather low methane conversion of about 1.5% under almost identical conditions.⁷ Pure ceria catalytically converts methane above 950 °C, and the initially poor product selectivities can be enhanced by tuning the methane gas flow (Figure S10). However, the CeO₂ catalyst rapidly deactivates

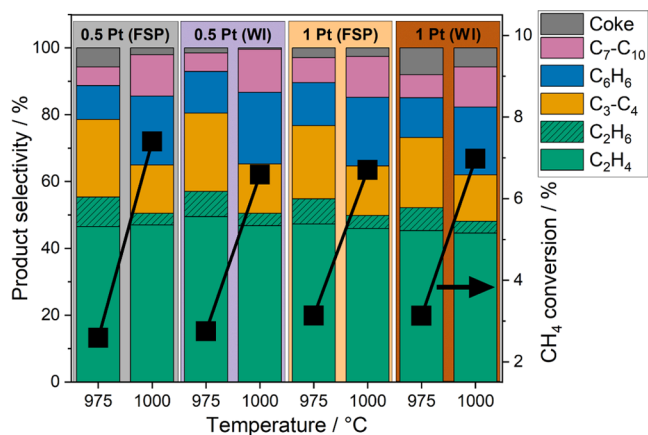


Figure 3. Product selectivities and CH₄ conversion for the nonoxidative CH₄ conversion over 0.5 and 1.0 wt % Pt/CeO₂ prepared via FSP and WI in 90% CH₄/N₂ as a function of reaction temperatures at 11.5 L/(g·h) (975 °C) and 13.5 L/(g·h) (1000 °C); black squares: CH₄ conversion and bar diagram: product selectivities (C₇–C₁₀ hydrocarbon fractions correspond to the sum of selectivity for toluene, xylene, and naphthalene).

due to coke formation. Strikingly, the coke selectivity can be reduced to less than 5% by doping ceria with platinum and simultaneously tuning the gas flow (Figure S11). Both Pt/CeO₂ catalysts exhibited high selectivity toward aromatics, typically higher than that reported in the literature.^{6,8,9,11,46–49} Furthermore, both tested systems showed high selectivity toward C₂ hydrocarbons and a stable performance within a 7 h time on stream (TOS) test (Figure S12). Methane conversion increased from about 3 to 7% upon increasing the reaction temperature from 975 to 1000 °C (Figure 3). The ethylene selectivity was nearly constant at about 45% for the two investigated reaction temperatures, whereas C₃–C₄ selectivity decreased and more aromatics were formed for 1000 °C in comparison to 975 °C. Interestingly, there was not much difference in the product distribution between the two samples. In comparison to the pure ceria catalyst (Figure S10), doping of Pt allowed lowering the reaction temperature to 975 °C while maintaining low coke formation rates. Moreover, the catalytic tests exhibited good reproducibility under the same conditions (for further details, cf. Figure S13 in the Supporting Information). Furthermore, no visible coke deposition was observed on the reactor walls after catalytic testing.

Neither the varied platinum loading nor the different preparation methods had a significant influence on the catalytic performance, even 1 Pt (FSP)_{ap} consisting of Pt nanoparticles (confirmed by XRD, Figure S1) showed similar catalytic activity.

By dosing pulses of methane over catalysts at the reaction temperature, the activation phase of direct methane conversion reactions can be studied in depth.^{50–52} Figure 4 shows a pulsed reaction study at 975 °C over the 0.5 Pt (FSP) catalyst. The initially decreasing C₂H₄/C₂H₆ signal increased from the 5th until the 18th pulse. At the same time, the initial high CO and H₂ formation continuously decreased. Moreover, significant amounts of CO₂ and H₂O only formed during the first two pulses. Thus, it seems that complete oxidation (CH₄ + [O] → CO₂ + H₂O) and partial oxidation of methane (CH₄ + [O] → CO + H₂) by ceria are competing reaction pathways during these first methane pulses.⁵³ The amount of C₆H₆ increased after the 7th and the signal maximum is reached at the 22nd pulse. Comparing the signal evolution of C₆H₆ to C₂H₄/C₂H₆,

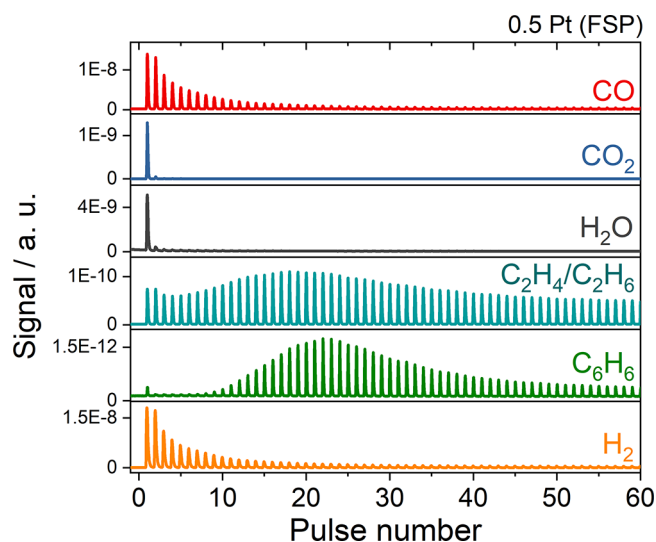


Figure 4. Pulsed reaction study of 0.5 Pt (FSP) at a reaction temperature of 975 °C and pulses of 5 mL 90% CH₄/He at a rate of 30 mL/min Ar carrier gas every 6 min.

C₆H₆ exhibits a postponed signal increase and maximum, most likely due to the formation of surface intermediates. Subsequently, both C₂H₄/C₂H₆ and C₆H₆ signals decreased and then stabilized around the 50th pulse. For both tested samples, increased amounts of C₂H₄ and C₆H₆ are only measured after CO and CO₂ formations decrease. This leads to the conclusion that first the ceria, which is in close contact with Pt, has to be reduced to form a Ce–Pt active phase enabling increased product formation. The nature of this active phase will be investigated in the following section with the help of *operando* XAS measurements. Based on the observations, the reaction of 0.5 Pt (FSP) can be divided into three phases. During the activation stage, the major part of the ceria reduction takes place, and the high CH₄ conversion of more than 80% decreases with every pulse (Figure S14a). This is followed by an induction period, where the formation of C₂-hydrocarbons and C₆H₆ initially increase with every pulse and subsequently decrease until a constant product yield is achieved, the stable running phase. Likewise, the CH₄ conversion rate also stabilizes (Figure S14a), which is well in line with the fixed-bed catalytic activity results. The duration of these stages correlates with the Pt loading and decreases for a higher amount of Pt (Figures S14b and 4). Kosinov et al.⁵³ reported similar phases during the MDA reaction over Mo/ZSM-5 catalysts. In line with our observations, Lykhach et al.¹⁸ reported that reduction of ceria upon methane activation is facilitated by hydrogen spillover from Pt particles to the ceria support. Similarly, Gänzler et al.⁵⁴ ascribed different activation temperatures during TPR of CO, H₂, and C₃H₆ for a Pt/CeO₂–Al₂O₃ catalyst to the critical role of the Pt–CeO₂ interface with varying Pt nanoparticle sizes.

3.3. Synchrotron-Based Vacuum Ultraviolet Photoionization Mass Spectrometry. Intermediate products of the direct nonoxidative conversion of methane over 0.5 Pt (FSP) at 1000 °C were identified by synchrotron-based vacuum ultraviolet photoionization mass spectrometry (SVUV-PIMS). Ionization at a photon energy of 10.6 eV, which is lower than the CH₄ ionization energy (12.6 eV), allows detection of intermediate radicals, e.g., methyl radicals, and products.^{55–58} The following gas-phase species were thereby identified by SVUV-PIMS (mass-to-charge-ratio (*m/z*)): methyl radicals

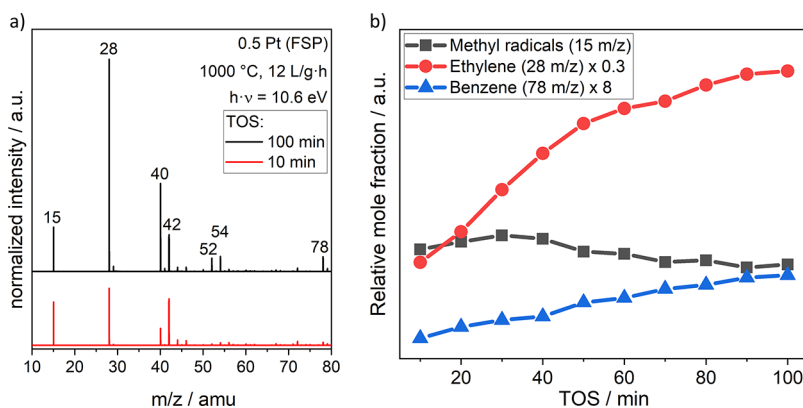


Figure 5. Gas-phase species in the reactor effluent over 0.5 Pt (FSP) detected by SVUV-PIMS (a) at 10 and 100 min TOS normalized to the 15 m/z peak and (b) relative integrated product peak intensities. Reaction conditions: 1000 °C, 45 mbar, and 12 L/(g·h) CH_4 ; measured products (m/z): methyl radical (15), C_2H_4 (28), C_3H_4 (40), C_3H_6 (42), C_4H_4 (52), C_4H_6 (54), and C_6H_6 (78).

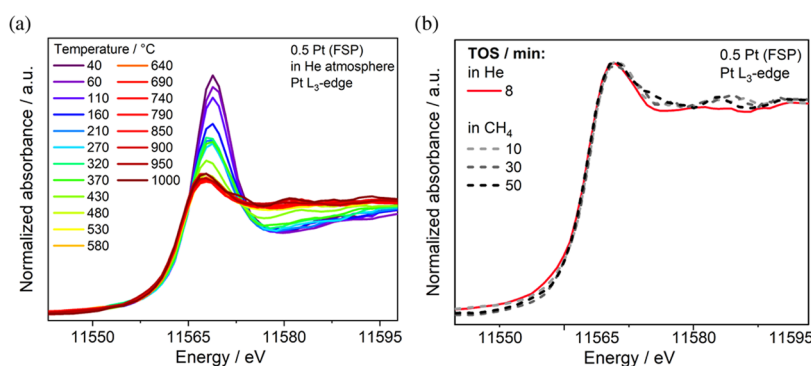


Figure 6. XANES spectra recorded at the Pt L_3 -edge of 0.5 Pt (FSP) (a) during heating up in He and (b) reaction at 975 °C in 90% CH_4/He upon 10 min TOS according to Figure S15 (cf. Figure S16 for corresponding MS signals).

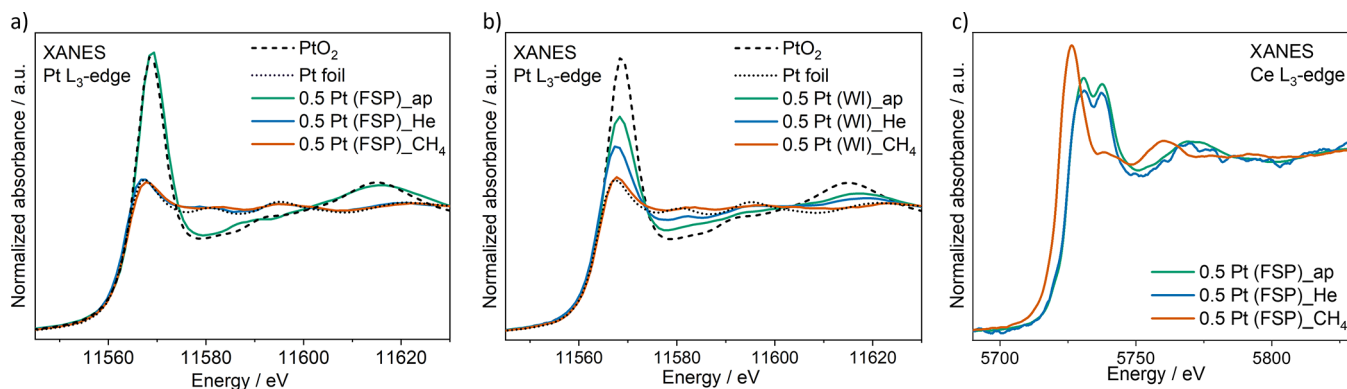


Figure 7. XANES spectra recorded at the Pt L_3 -edge of (a) 0.5 Pt (FSP), (b) 0.5 FSP (WI), and (c) at the Ce L_3 -edge of 0.5 Pt (FSP); measured at 40 °C after the following treatment: as-prepared (_ap), He treatment (_He), and after 1h *operando* reaction (_ CH_4) according to Figure S15 (cf. Figure S16 for corresponding MS signals).

(15), C_2H_4 (28), C_3H_4 (40), C_3H_6 (42), C_4H_4 (52), C_4H_6 (54), C_6H_6 (78) (Figure 5a). Similar products were observed for Fe single sites on SiO_2 by activating CH_4 in the absence of oxidants.⁶ A reaction pathway was proposed including the generation of methyl radicals that desorb and form ethylene as the main product, benzene, and naphthalene through gas-phase reactions, which can also be assumed for the Pt/ CeO_2 catalysts studied in this work.

The activation period revealed by the pulsed reaction study in Figure 4 can also be seen in the SVUV-PIMS experiment as the increase of benzene and ethylene formation with increasing TOS (Figure 5b). Furthermore, both ethylene and benzene

formations showed a similar increase until 50 min TOS, whereas, at the end of the experiment (100 min TOS), the relative increase of ethylene is about twofold and thereby lower than that of benzene (about threefold).

3.4. X-ray Absorption Spectroscopy. To shed more light on the chemical state of the catalytically active platinum species and cerium, *operando* XAS was conducted at the Pt L_3 -edge and Ce L_3 -edge on 0.5 Pt (FSP) and at the Pt L_3 -edge on 0.5 Pt (WI) at the high-temperature reaction conditions. The *operando* measurement procedure is shown in Figure S15. The XANES spectrum of the as-prepared 0.5 Pt (FSP) catalyst is similar to that of PtO_2 (Figure 6a, spectrum marked with “_ap” in Figure

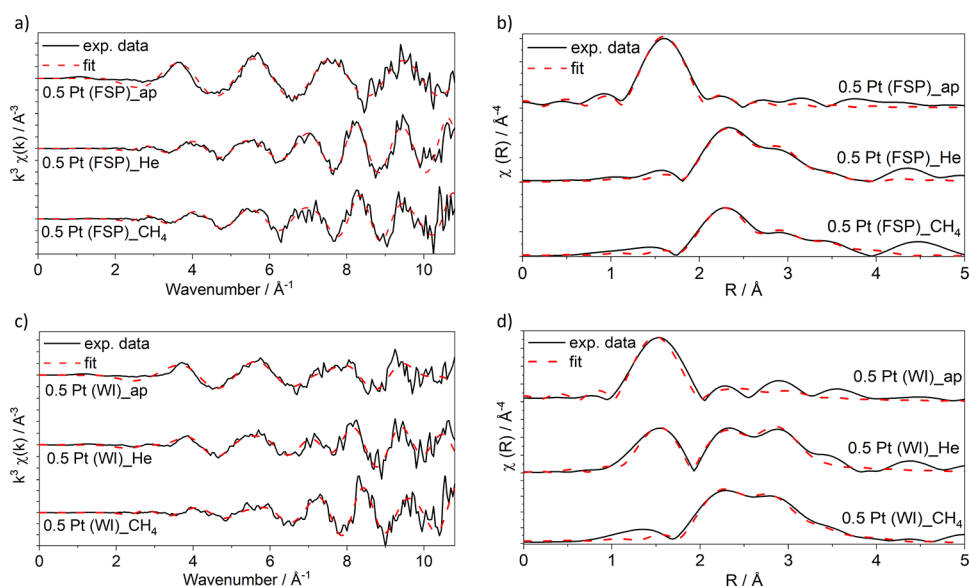


Figure 8. EXAFS spectra of 0.5 Pt (FSP) and 0.5 Pt (WI) [solid lines] as well as corresponding EXAFS fitting [dashed lines] in the k -space (a, resp. c) and R -space (b, resp. d) recorded at the Pt L_{3} -edge and 40 °C after the following treatment: as prepared (_ap), He treatment (_He), and after 1h *operando* reaction (_CH₄) according to Figure S15. Note that the R -space is not corrected for phase shift.

Table 1. EXAFS Fitting Results for 0.5 Pt (FSP) and 0.5 FSP (WI) Catalysts

| sample name | path | R (Å) | CN | σ^2 (Å ²) | E_0 (eV) | R-factor |
|------------------------------|--------------------|--------------------------|------------------------|------------------------------|------------|----------|
| 0.5 Pt (FSP)_ap | Pt–O | 2.00 ± 0.01 | 5.8 ± 0.7 | 0.0017 ± 0.0006 | 9.9 ± 2.0 | 0.0040 |
| 0.5 Pt (FSP)_He | Pt–Pt ₁ | 2.74 ± 0.01 | 9.9 ± 0.8 | 0.004 ^a | 6.4 ± 1.6 | 0.0035 |
| | Pt–Ce | 2.98 ± 0.05 | 0.9 ± 0.7 | 0.004 ^a | | |
| | Pt–Pt ₂ | 3.90 ± 0.05 ^b | 3.0 ± 2.4 ^b | 0.006 ^a | | |
| 0.5 Pt (FSP)_CH ₄ | Pt–Pt ₁ | 2.73 ± 0.02 | 9.0 ± 1.0 | 0.004 ^a | 6.8 ± 2.1 | 0.0085 |
| | Pt–Ce | 2.94 ± 0.04 | 2.0 ± 0.8 | 0.004 ^a | | |
| | Pt–Pt ₂ | 3.84 ± 0.03 ^b | 5.3 ± 2.8 ^b | 0.006 ^a | | |
| 0.5 Pt (WI)_ap | Pt–O | 1.98 ± 0.02 | 3.8 ± 0.7 | 0.002 ^a | 7.7 ± 2.9 | 0.0237 |
| | Pt–Pt ₁ | 2.79 ± 0.03 | 3.0 ± 0.9 | 0.004 ^a | | |
| 0.5 Pt (WI)_He | Pt–O | 1.94 ± 0.02 | 2.3 ± 0.4 | 0.002 ^a | 4.2 ± 2.1 | 0.0202 |
| | Pt–Pt ₁ | 2.73 ± 0.02 | 4.8 ± 1.0 | 0.004 ^a | | |
| | Pt–Ce | 3.13 ± 0.03 ^b | 1.8 ± 0.8 ^b | 0.004 ^a | | |
| 0.5 (WI)_CH ₄ | Pt–Pt ₁ | 2.66 ± 0.01 | 7.7 ± 0.7 | 0.004 ^a | 4.9 ± 1.6 | 0.0054 |
| | Pt–Ce | 3.09 ± 0.04 ^b | 1.2 ± 0.7 | 0.004 ^a | | |
| | Pt–Pt ₂ | 3.82 ± 0.02 ^b | 5.4 ± 1.8 ^b | 0.006 ^a | | |

^aTreatment conditions: as prepared (_ap), after He treatment (_He), and after 1h reaction (_CH₄) according to Figure S15. Values were fixed.

^bValues were fitted with restraints based on structural information (for further details, cf. the Supporting Information).

7a), hinting at an almost completely oxidized state of Pt at this stage. During heating to a reaction temperature in a He atmosphere, the XANES spectra in Figure 6a converted stepwise in two temperature regimes to a state very similar to metallic Pt, indicating the autoreduction of the Pt single sites. As observed by a decrease of white line intensity, the platinum was fully reduced already at 530 °C. This might be due to the Pt single sites being located at unfavorable facets and being bound only weakly, thereby not able to resist sintering to metallic nanoparticles.⁵⁹ Linear combination fitting of the XANES data (Figure S17 and Table S2) and thermogravimetric analysis (TGA, Figure S18) evidenced two reduction regimes from about 50 to 250 °C and 400 to 530 °C, most likely corresponding to the reduction of atomically dispersed Pt^{IV}O₂ to Pt^{II}O and subsequent reduction to Pt⁰ nanoparticles, respectively.⁶⁰ This could be the reason for a small amount of coke formation (Figure 3), as reported by Xie et al.⁹ The *operando* XANES spectra of 0.5 Pt (FSP) in Figure 6b during the

reaction with CH₄ at 975 °C revealed near-edge features similar to a Ce–Pt alloy (compared to CePt₅ reference, cf. the later section), hinting toward an increased Pt–Ce interaction. Hydrogen, ethylene, ethane, and benzene were detected as reaction products (MS, Figure S16). These changes in the XANES spectra are still present after cooling to room temperature in Figure 7a (denoted 0.5 Pt (FSP)_CH₄) and will be interpreted hereafter with EXAFS fitting and modeling of XANES spectra.

The XANES spectrum at the Ce L_{3} -edge of the 0.5 Pt (FSP) catalyst shows that the oxidation state of bulk ceria is maintained throughout the He pretreatment; a surface reduction probably occurs as outlined earlier.^{61,62} However, after reaction with CH₄, the spectrum resembles those of the Ce³⁺ species, e.g., cerium(III)nitrate,⁵⁴ and shows a shift of the absorption edge energy from 5724.5 to 5721.7 eV, indicating a reduction of bulk CeO₂ to Ce³⁺ (Figure 7c). It was shown previously that doping of platinum increases the formation of catalytically active Ce³⁺

sites at the interface with ceria for oxidation of carbon monoxide.⁶³ Also, Gänzler et al.⁵⁴ showed that by adding Pt, the reducibility of CeO₂ surface sites, which are in close contact with Pt, improves. However, no Ce₂O₃ XRD reflections of the spent catalysts studied were visible, most probably because Pt/Ce₂O₃ easily reoxidizes in air (Figure S1).

Incipient wetness impregnation leads to Pt aggregates including atomically dispersed Pt and the Pt L₃ XANES spectrum of the as-prepared catalyst (0.5 Pt (WI)_ap) indicated only an approximately 56% oxidized state according to the linear combination fitting (LCF, using Pt metal and PtO₂ as references) of the XANES spectra (Figure 7b, Table S3 and Figure S19). In contrast to the FSP prepared sample, heating in He only partly reduced the WI prepared catalyst to a remaining 30% Pt⁴⁺ state (spectrum marked with “_He”). The activation of the Pt nanoparticles with CH₄ at 975 °C led to a full reduction of Pt. Moreover, the fine structure of the XANES spectrum became similar to the one of the FSP sample, also indicating increased Pt–Ce interaction.

The Pt L₃ EXAFS analysis based on the comparison of the experimental data with Pt and PtO₂ reference data was performed for both catalysts at three different conditions. The backscattering contributions in Fourier-transformed EXAFS data at about 1.7 Å and at 2.3/3.5 Å (not corrected for the phase shift) can be attributed to Pt⁴⁺–O and Pt⁰–Pt₁/Pt⁰–Pt₂ backscattering, respectively (Figure S20). Both as-prepared catalysts showed a significant Pt⁴⁺–O backscattering peak in Figure 8b,d. The Pt single sites of the as-prepared 0.5 Pt (FSP) catalyst appeared highly dispersed, as indicated by the absence of Pt–Pt scattering in the EXAFS data (Figure 8a,b and Table 1).¹⁴ After the He treatment (curves marked with “_He” in Figure 8), backscattering peaks at Pt⁰–Pt₁ and Pt⁰–Pt₂ appeared and Pt⁴⁺–O scattering decreased for both samples, the latter one less pronounced in the WI catalyst. Subsequent reaction with methane resulted in a slightly less-pronounced backscattering at 2.9 Å for the FSP sample (graph marked with “_CH₄”), which will be investigated in detail with EXAFS fitting. The WI sample showed a significant decrease of the Pt⁴⁺–O backscattering after the reaction. These findings are well in line with the interpretation of the *operando* XANES measurements.

To determine the Pt environment of the activated catalysts and follow the possible Ce–Pt alloy formation, backscattering paths from different Pt and Ce phases were fitted to the EXAFS data (Figure S21 and Table S4). After heating in He, the structure of 0.5 Pt (FSP) is very close to metallic Pt and the addition of Pt–Ce scattering is not mandatory to achieve a good fit (0.5 Pt (FSP)_He-C and _He-D, Figure S21 and Table S4). In contrast, including the Pt–Ce scattering significantly improves the fit for 0.5 Pt (FSP)_CH₄ (Table 1; _CH₄-A, -B, and -C in Figure S21 and Table S4). This indicates a strong metal–support interaction (SMSI) in the FSP catalyst after reaction with CH₄, which was reported to be accompanied by decoration and/or encapsulation of the Pt particles by the CeO₂/Ce₂O₃ support or the formation of a Ce–Pt alloy.^{20,21,64} Chen et al.⁶⁵ reported similar results by reducing Pt single-site catalysts at 975 °C in H₂ and thereby observed the sintering to nanoparticles of about 15 nm size covered by a CeO_x overlayer. After reaction with methane (0.5 Pt (FSP)_CH₄), the Pt–Ce coordination number increased by approximately 1 and the Pt–Ce bond length decreased by about 0.04 Å, indicating an increased Pt–Ce interaction.

The EXAFS fitting of the data recorded for the WI prepared catalyst after the He treatment (0.5 Pt (WI)_He) and reaction

(0.5 Pt (WI)_CH₄) revealed a similar but less-defined structure of Pt species compared to FSP prepared samples. This is likely the reason for the similar catalytic performance observed for FSP and WI samples. Generally, the coordination numbers appear lower comparing the WI prepared with the FSP prepared catalyst. After the reaction with CH₄, Pt–Pt₁ and Pt–Ce coordination numbers decrease and the calculated Pt–Pt₁ and Pt–Ce bond lengths of the WI prepared sample become more similar to the ones for the CePt₅ configuration.⁴⁰ Comparing the WI prepared sample to the FSP prepared catalyst, hints toward smaller Pt nanoparticles, a weakened Pt–Ce interaction, and less decoration or encapsulation of Pt by ceria (0.5 Pt (WI)_CH₄; Table 1). The average spherical particle sizes estimated from EXAFS fitting of the first-shell Pt–Pt coordination number⁶⁶ are 1.5–2.7 nm for 0.5 Pt (FSP)_CH₄ and 1.2–1.6 nm for the 0.5 Pt (WI)_CH₄ sample. These values are significantly smaller than those seen in TEM (Figure S4). The possible reason for this difference in the estimated particle size is the formation of TEM-invisible species and/or flat species, as shown by the TEM images, due to the wetting of Pt nanoparticles on ceria under SMSI in contrast to spherical particles assumed in EXAFS analysis.⁶⁷ The *ex situ* XAS results and EXAFS fitting of *post mortem* 0.5 Pt (FSP) (Figures S22, S23, and Table S5) confirmed that Pt is not easily reoxidized in air and the established SMSI is preserved after the reaction with CH₄.

Starting from two differently composed Pt/CeO₂ catalysts in terms of Pt oxidation and dispersion state, activation in He leads to different states of Pt reduction. After reaction with CH₄, cationic Pt single sites (FSP sample) as well as Pt aggregates including single sites (WI sample) sinter to Pt nanoparticles decorated by ceria or form a Ce–Pt alloy phase, which is accompanied by a reduction of Ce⁴⁺ bulk ceria to Ce³⁺. According to EXAFS results, the FSP sample shows larger Pt nanoparticles than the WI sample. In summary, we observe that in addition to earlier reports,⁹ outlining single-atom Pt sites as active species, also Pt nanoparticles strongly interacting with Ce can contribute to the direct conversion of CH₄. The Pt/CeO₂ single-site catalysts were found to strongly change under reaction conditions either forming encapsulated Pt nanoparticles or Ce–Pt alloy due to strong Pt–Ce interaction. The SVUV-PIMS results and the pulsed-reaction studies show that ceria first has to be reduced to enable an additional pathway to increased product formation rates. As a first step, the formed Pt–Ce interface allows the activation of CH₄ by forming methyl radicals, which then react further in the gas phase. In addition, this reduces the coke formation, similar to the iron single-site catalyst Fe@SiO₂.⁶ Ding et al.⁴⁵ reported catalytic carbon monoxide oxidation and water–gas shift reaction over Pt nanoparticles on SiO₂, whereas Pt single sites behaved as spectators. Furthermore, Maurer et al.¹³ showed that the catalytic activity of Pt²⁺ single sites for CO, C₃H₆, and CH₄ oxidation increases after generating Pt_x^{dt} clusters. These clusters can be reoxidized and redispersed, proving the highly dynamic nature of these Pt sites.

For all tested catalysts, pronounced changes in shape and position of the XANES features at the Pt L₃-edge were observed. In Figure 9, the XANES spectra of 0.5 Pt (WI) and 0.5 Pt (FSP) after reaction with CH₄ are displayed together with the XANES spectrum of the Pt foil and CePt₅ reference material. Unfortunately, LCF with the CePt₅ reference is not feasible since the XRD of CePt₅ showed impurities of metallic Pt (Figure S2). The post-edge features B and C of the samples after reaction and CePt₅ are shifted to higher energies and are less pronounced

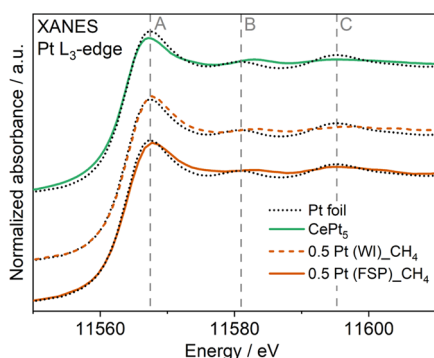


Figure 9. XANES spectra recorded at the Pt L_{3} -edge of Pt references, 0.5 Pt (FSP) $_{CH_4}$ and 0.5 Pt (WI) $_{CH_4}$ after 1h reaction according to Figure S15 with distinct features of the Pt foil marked with dashed lines and labeled A–C.

in comparison to the Pt foil, whereas feature A is fairly similar to the Pt foil for both catalysts.

Similar changes were seen by modeling of Pt XANES for small platinum clusters (about 10 atoms cluster size) supported on CeO_2 and were attributed to X-ray absorption contributed from Pt sites next to Pt in contrast to Pt sites next to Pt and Ce.⁶⁸

To clarify this behavior, XANES simulations using the FEFF9 code⁴³ of several Ce–Pt alloys were performed. The near-edge absorption features of Ce–Pt alloys resemble the experimental data best for compounds with only Pt in the first shell (Figure 10a,b).⁴³ The consistency with the measured spectra, especially for the energy shift of the B and C feature in Figure 9, reduces with decreasing Pt–Pt₁ and increasing Pt–Ce₁ first shell coordination number (Figure 10c–f). This is well in line with

the EXAFS fitting results. Since the near-edge XANES features are reflected differently well between $CePt_5$, $CePt_2$, and Ce_3Pt_4 , the observed Pt–Ce interaction and alloy formation might be a mixture of these phases.

4. CONCLUSIONS

In this study, two sets of 0.5–1% Pt-doped CeO_2 catalysts were prepared with different Pt dispersion and oxidation state. Both the FSP prepared Pt single-site catalysts and the WI prepared catalysts with aggregated Pt clusters and Pt single sites showed similar catalytic activity and selectivity for the direct non-oxidative conversion of methane, exceeding the catalytic activity of pure ceria. The catalyst structure fate of the Pt single sites was studied by a set of complementary characterization techniques. Detailed structural evolution under reaction conditions was carefully investigated with *operando* XAS up to the high temperature regime using a new in-house built setup. Heating in an inert gas atmosphere leads to autoreduction of the oxidized Pt single sites in the FSP sample and sintering of the Pt sites to form some Pt nanoparticles/clusters. Comparing the resulting XANES spectra to modeled ones confirms an increased Pt–Ce interaction and possibly alloy formation upon CH_4 conversion at the reaction temperature. Furthermore, EXAFS fitting unraveled a significant Pt–Ce contribution, indicating decoration and encapsulation of the Pt particles by CeO_x or a partial Ce–Pt alloy formation.

Investigation of the catalyst and the reaction during CH_4 pulses at the reaction temperature unraveled three reaction stages: reduction of the ceria support during activation, induction phase with increased product formation, and, finally, stable running. Hence, the reduction of bulk ceria is correlated

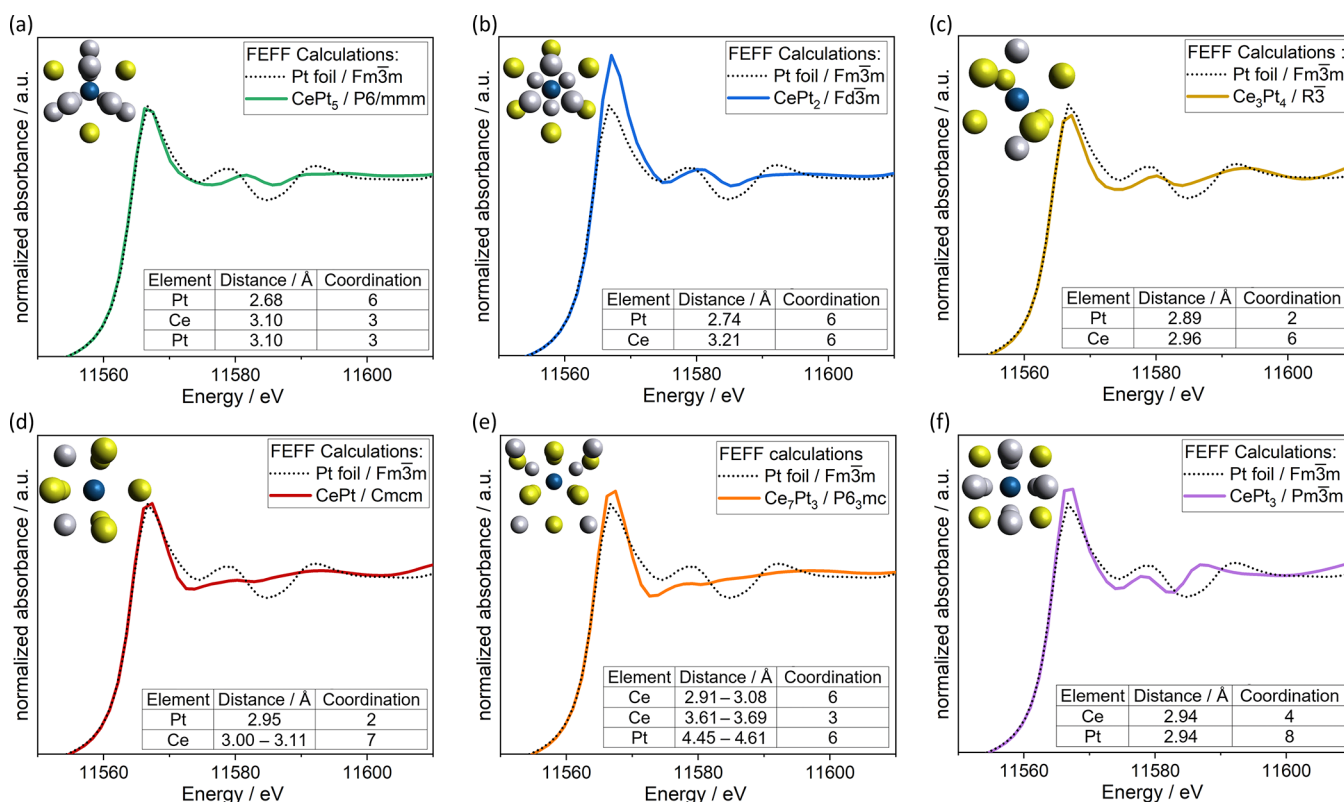


Figure 10. (a–f) FEFF9-simulated XANES spectra of the Pt foil, $CePt_5$, $CePt_2$, Ce_3Pt_4 , $CePt$, Ce_7Pt_3 , and $CePt_3$ with a table of neighbors to the central Pt atom and an inset of models showing the first 2 shells (Pt: gray, Ce: yellow) to the central Pt atom (blue).

with increased product formation. Moreover, methyl radicals were detected as reaction intermediates indicating the presence of a reaction pathway through the gas-phase coupling of radicals.

Starting from two differently composed sets of catalysts, with respect to Pt oxidation and dispersion state, a similar structural configuration after reaction with CH₄ was observed. We propose that apart from single-atom Pt sites, the Pt–Ce interface with Pt nanoparticles either alloyed with Ce, encapsulated, or directly connected to the partially reduced ceria support on the CeO₂ overlayers contribute to enhanced catalytic activity in the direct nonoxidative conversion of methane. The results reveal detailed structural evolution of the Pt/CeO₂ active sites under those demanding reaction conditions. These findings may help in the future to systematically optimize industrially relevant parameters such as the reaction temperature and catalyst loading.

■ ASSOCIATED CONTENT

SI Supporting Information

The Supporting Information is available free of charge at <https://pubs.acs.org/doi/10.1021/acscatal.2c00092>.

N₂ physisorption, X-ray diffraction, TEM, CO-DRIFTS, and Raman spectroscopy measurements; results of temperature-programmed reduction; catalytic activity and pulsed reaction studies; results of synchrotron-based vacuum ultraviolet photoionization mass spectrometry; details on XAS measurements including *operando* XAS measurement procedure, mass spectrometry product gas analysis, XANES/thermogravimetric studies, LCF, and EXAFS fitting results and exemplary FEFF input file (PDF)

■ AUTHOR INFORMATION

Corresponding Authors

Xiulian Pan – State Key Laboratory of Catalysis, National Laboratory for Clean Energy, 2011-Collaborative Innovation Center of Chemistry for Energy Materials, Dalian Institute of Chemical Physics, Chinese Academy of Sciences, 116023 Dalian, China; orcid.org/0000-0002-5906-6675; Email: panxl@dicp.ac.cn

Jan-Dierk Grunwaldt – Institute for Chemical Technology and Polymer Chemistry (ITCP), Karlsruhe Institute of Technology (KIT), 76131 Karlsruhe, Germany; Institute of Catalysis Research and Technology (IKFT), Karlsruhe Institute of Technology (KIT), 76344 Eggenstein-Leopoldshafen, Germany; orcid.org/0000-0003-3606-0956; Email: grunwaldt@kit.edu

Authors

Daniel Eggart – Institute for Chemical Technology and Polymer Chemistry (ITCP), Karlsruhe Institute of Technology (KIT), 76131 Karlsruhe, Germany; orcid.org/0000-0002-3083-2903

Xin Huang – State Key Laboratory of Catalysis, National Laboratory for Clean Energy, 2011-Collaborative Innovation Center of Chemistry for Energy Materials, Dalian Institute of Chemical Physics, Chinese Academy of Sciences, 116023 Dalian, China

Anna Zimina – Institute for Chemical Technology and Polymer Chemistry (ITCP), Karlsruhe Institute of Technology (KIT), 76131 Karlsruhe, Germany; Institute of Catalysis Research and Technology (IKFT), Karlsruhe Institute of Technology

(KIT), 76344 Eggenstein-Leopoldshafen, Germany;

orcid.org/0000-0002-3111-7741

Jiuzhong Yang – National Synchrotron Radiation Laboratory, University of Science and Technology of China, 230029 Hefei, China; orcid.org/0000-0002-7076-3412

Yang Pan – National Synchrotron Radiation Laboratory, University of Science and Technology of China, 230029 Hefei, China; orcid.org/0000-0002-9360-3809

Complete contact information is available at: <https://pubs.acs.org/doi/10.1021/acscatal.2c00092>

Author Contributions

[†]D.E. and X.H. contributed equally. The manuscript was written through contributions of all authors. All authors have given approval to the final version of the manuscript.

Notes

The authors declare no competing financial interest.

■ ACKNOWLEDGMENTS

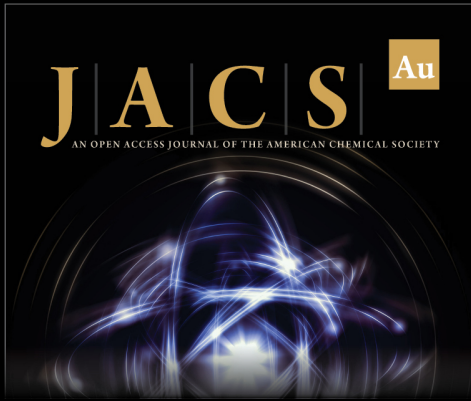
This work was supported by a Sino-German DFG-grant (GR 3987/9-1) and grants for equipment (Raman spectrometer, INST 121384/73-1; High-Output Catalyst Development Platform, INST 121384/16-1, and thermal analysis equipment, INST 121384/73-1), by the National Natural Science Foundation of China (Grant Nos. 21761132035 and 21805300), and 65th batch of China Postdoctoral Science Foundation (2019M651159). Part of this research was carried out at the light source PETRA III at DESY, a member of the Helmholtz Association (HGF). The authors would like to thank Edmund Welter and Ruidy Nemausat for their assistance in using beamline P65. The authors acknowledge the Karlsruhe Nano Micro Facility (KNMF, <http://www.kit.edu/knmf>) of the Forschungszentrum Karlsruhe for provision of access to instruments at their laboratories. Furthermore, the authors thank Dr. Thomas Bergfeldt (IAM-AWP/KIT) for ICP-OES measurements, Xiaohui Huang (INT/KIT) for TEM measurements, Dr. Maria Casapu (ITCP/KIT) for thermoanalytical measurements, Dr. Dmitry Doronkin (ITCP/KIT) for discussion on EXAFS fitting, and Dr. Alexey Boubnov for discussion on simulated XANES spectra. The authors are also grateful to Dr. Gülperi Nails (ITCP/KIT) and Deniz Zengel (ITCP/KIT) for beamtime support and to Prof. Xuezhi Duan (School of Chemical Engineering of East China University of Science and Technology) for fruitful discussion on the fixed bed reaction and the mass transfer in fixed bed reactors.

■ REFERENCES

- (1) Schwach, P.; Pan, X.; Bao, X. Direct conversion of methane to value-added chemicals over heterogeneous catalysts: challenges and prospects. *Chem. Rev.* **2017**, *117*, 8497–8520.
- (2) Economides, M. J.; Wood, D. A. The state of natural gas. *J. Nat. Gas. Sci. Eng.* **2009**, *1*, 1–13.
- (3) Keller, G.; Bhasin, M. Synthesis of ethylene via oxidative coupling of methane: I. determination of active catalysts. *J. Catal.* **1982**, *73*, 9–19.
- (4) Wang, L.; Tao, L.; Xie, M.; Xu, G.; Huang, J.; Xu, Y. Dehydrogenation and aromatization of methane under non-oxidizing conditions. *Catal. Lett.* **1993**, *21*, 35–41.
- (5) Huang, X.; Jiao, X.; Lin, M.; Wang, K.; Jia, L.; Hou, B.; Li, D. Coke distribution determines the lifespan of a hollow Mo/HZSM-5 capsule catalyst in CH₄ dehydroaromatization. *Catal. Sci. Technol.* **2018**, *8*, 5740–5749.
- (6) Guo, X.; Fang, G.; Li, G.; Ma, H.; Fan, H.; Yu, L.; Ma, C.; Wu, X.; Deng, D.; Wei, M.; Tan, D.; Si, R.; Zhang, S.; Li, J.; Sun, L.; Tang, Z.;

- Pan, X.; Bao, X. Direct, nonoxidative conversion of methane to ethylene, aromatics, and hydrogen. *Science* **2014**, *344*, 616–619.
- (7) Hao, J.; Schwach, P.; Fang, G.; Guo, X.; Zhang, H.; Shen, H.; Huang, X.; Eggart, D.; Pan, X.; Bao, X. Enhanced methane conversion to olefins and aromatics by H-donor molecules under non-oxidative condition. *ACS Catal.* **2019**, *9*, 9045–9050.
- (8) Han, S. J.; Lee, S. W.; Kim, H. W.; Kim, S. K.; Kim, Y. T. Non-oxidative direct conversion of methane on silica-based iron catalysts: effect of catalytic surface. *ACS Catal.* **2019**, *9*, 7984–7997.
- (9) Xie, P.; Pu, T.; Nie, A.; Hwang, S.; Purdy, S. C.; Yu, W.; Su, D.; Miller, J. T.; Wang, C. Nanoceria supported single-atom platinum catalysts for direct methane conversion. *ACS Catal.* **2018**, *8*, 4044–4048.
- (10) Wen, J.-H.; Wang, G.-C. Methane non-oxidative direct conversion to C₂ hydrogenations over CeO₂-supported Pt catalysts: a DFT study. *J. Phys. Chem. C* **2020**, *124*, 13249–13262.
- (11) Bajec, D.; Kostyniuk, A.; Pohar, A.; Likozar, B. Micro-kinetics of non-oxidative methane coupling to ethylene over Pt/CeO₂ catalyst. *Chem. Eng. J.* **2020**, *396*, No. 125182.
- (12) Jeong, H.; Kwon, O.; Kim, B.-S.; Bae, J.; Shin, S.; Kim, H.-E.; Kim, J.; Lee, H. Highly durable metal ensemble catalysts with full dispersion for automotive applications beyond single-atom catalysts. *Nat. Catal.* **2020**, *3*, 368–375.
- (13) Maurer, F.; Jelic, J.; Wang, J.; Gänzler, A.; Dolcet, P.; Wöll, C.; Wang, Y.; Studt, F.; Casapu, M.; Grunwaldt, J.-D. Tracking the formation, fate and consequence for catalytic activity of Pt single sites on CeO₂. *Nat. Catal.* **2020**, *3*, 824–833.
- (14) Kottwitz, M.; Li, Y.; Palomino, R. M.; Liu, Z.; Wang, G.; Wu, Q.; Huang, J.; Timoshenko, J.; Senanayake, S. D.; Balasubramanian, M.; et al. Local structure and electronic state of atomically dispersed Pt supported on nanosized CeO₂. *ACS Catal.* **2019**, *9*, 8738–8748.
- (15) Stadnichenko, A. I.; Muravev, V. V.; Koscheev, S. V.; Zaikovskii, V. I.; Aleksandrov, H. A.; Neyman, K. M.; Boronin, A. I. Study of active surface centers of Pt/CeO₂ catalysts prepared using radio-frequency plasma sputtering technique. *Surf. Sci.* **2019**, *679*, 273–283.
- (16) Derevyannikova, E. A.; Kardash, T. Y.; Stadnichenko, A. I.; Stonkus, O. A.; Slavinskaya, E. M.; Svetlichnyi, V. A.; Boronin, A. I. Structural insight into strong Pt–CeO₂ interaction: from single Pt atoms to PtO_x clusters. *J. Phys. Chem. C* **2019**, *123*, 1320–1334.
- (17) Ye, X.; Wang, H.; Lin, Y.; Liu, X.; Cao, L.; Gu, J.; Lu, J. Insight of the stability and activity of platinum single atoms on ceria. *Nano Res.* **2019**, *12*, 1401–1409.
- (18) Lykhach, Y.; Staudt, T.; Lorenz, M. P. A.; Streber, R.; Bayer, A.; Steinrück, H. P.; Libuda, J. Microscopic insights into methane activation and related processes on Pt/ceria model catalysts. *ChemPhysChem* **2010**, *11*, 1496–1504.
- (19) Tauster, S.; Fung, S.; Garten, R. L. Strong metal-support interactions. Group 8 noble metals supported on titanium dioxide. *J. Am. Chem. Soc.* **1978**, *100*, 170–175.
- (20) Meriaudeau, P.; Dutel, J.; Dufaux, M.; Naccache, C. Further Investigation on Metal-Support Interaction: TiO₂, CeO₂, SiO₂ Supported Platinum Catalysts. In *Studies in Surface Science and Catalysis*; Elsevier, 1982; Vol. 11, pp 95–104.
- (21) Bernal, S.; Calvino, J.; Cauqui, M.; Gatica, J.; Lares, C.; Omil, J. P.; Pintado, J. Some recent results on metal/support interaction effects in NM/CeO₂ (NM: noble metal) catalysts. *Catal. Today* **1999**, *50*, 175–206.
- (22) Cavusoglu, G.; Miao, D.; Lichtenberg, H.; Carvalho, H. W.; Xu, H.; Goldbach, A.; Grunwaldt, J.-D. Structure and activity of flame made ceria supported Rh and Pt water gas shift catalysts. *Appl. Catal. A* **2015**, *504*, 381–390.
- (23) Lott, P.; Eck, M.; Doronkin, D. E.; Popescu, R.; Casapu, M.; Grunwaldt, J.-D.; Deutschmann, O. Regeneration of sulfur poisoned Pd–Pt/CeO₂–ZrO₂–Y₂O₃–La₂O₃ and Pd–Pt/Al₂O₃ methane oxidation catalysts. *Top. Catal.* **2019**, *62*, 164–171.
- (24) Tepluchin, M.; Casapu, M.; Boubnov, A.; Lichtenberg, H.; Wang, D.; Kureti, S.; Grunwaldt, J. D. Fe and Mn-based catalysts supported on γ-Al₂O₃ for CO oxidation under O₂-rich conditions. *ChemCatChem* **2014**, *6*, 1763–1773.
- (25) Kleist, W.; Grunwaldt, J.-D. High Output Catalyst Development in Heterogeneous Gas Phase Catalysis. In *Modern Applications of High Throughput R&D in Heterogeneous Catalysis*; Bentham Science Publishers, 2014; pp 357–371.
- (26) Schneider, C. A.; Rasband, W. S.; Eliceiri, K. W. NIH Image to ImageJ: 25 years of image analysis. *Nat. Methods* **2012**, *9*, 671–675.
- (27) Ohnishi, R.; Liu, S.; Dong, Q.; Wang, L.; Ichikawa, M. Catalytic dehydrocondensation of methane with CO and CO₂ toward benzene and naphthalene on Mo/HZSM-5 and Fe/Co-modified Mo/HZSM-5. *J. Catal.* **1999**, *182*, 92–103.
- (28) Zhang, Y.; Cao, C.; Li, Y.; Yuan, W.; Yang, X.; Yang, J.; Qi, F.; Huang, T.-P.; Lee, Y.-Y. Pyrolysis of n-butylbenzene at various pressures: influence of long side-chain structure on alkylbenzene pyrolysis. *Energy Fuels* **2017**, *31*, 14270–14279.
- (29) Luo, L.; You, R.; Liu, Y.; Yang, J.; Zhu, Y.; Wen, W.; Pan, Y.; Qi, F.; Huang, W. Gas-phase reaction network of Li/MgO-catalyzed oxidative coupling of methane and oxidative dehydrogenation of ethane. *ACS Catal.* **2019**, *9*, 2514–2520.
- (30) Wen, W.; Yu, S.; Zhou, C.; Ma, H.; Zhou, Z.; Cao, C.; Yang, J.; Xu, M.; Qi, F.; Zhang, G.; Pan, Y. Formation and fate of formaldehyde in methanol-to-hydrocarbon reaction: in situ synchrotron radiation photoionization mass spectrometry study. *Angew. Chem., Int. Ed.* **2020**, *59*, 4873–4878.
- (31) Cool, T. A.; Nakajima, K.; Taatjes, C. A.; McIlroy, A.; Westmoreland, P. R.; Law, M. E.; Morel, A. Studies of a fuel-rich propane flame with photoionization mass spectrometry. *Proc. Combust. Inst.* **2005**, *30*, 1681–1688.
- (32) Welter, E.; Chernikov, R.; Herrmann, M.; Nemausat, R. In *A Beamline for Bulk Sample X-ray Absorption Spectroscopy at the High Brilliance Storage Ring PETRA III*, AIP Conference Proceedings, AIP Publishing LLC, 2019; 040002.
- (33) Eggart, D.; Zimina, A.; Cavusoglu, G.; Casapu, M.; Doronkin, D. E.; Lomachenko, K. A.; Grunwaldt, J.-D. Versatile and high temperature spectroscopic cell for operando fluorescence and transmission x-ray absorption spectroscopic studies of heterogeneous catalysts. *Rev. Sci. Instrum.* **2021**, *92*, No. 023106.
- (34) Ravel, B.; Newville, M. ATHENA, ARTEMIS, HEPHAESTUS: data analysis for X-ray absorption spectroscopy using IFEFFIT. *J. Synchrotron Rad.* **2005**, *12*, 537–541.
- (35) Rehr, J. J.; Albers, R. C. Theoretical approaches to x-ray absorption fine structure. *Rev. Mod. Phys.* **2000**, *72*, 621.
- (36) Wyckoff, R. W. G. *Crystal structures 1*, 2nd ed.; Interscience Publishers: New York, 1963; Vol. 1, pp 7–83.
- (37) Siegel, S.; Hoekstra, H. R.; Tani, B. S. The crystal structure of beta-platinum dioxide. *J. Inorg. Nucl. Chem.* **1969**, *31*, 3803–3807.
- (38) Palenzona, A. Crystal structure and lattice constants of R₃Pt₄ compounds. *J. Less-Common Met.* **1977**, *53*, 133–136.
- (39) Gómez Sal, J.; Espeso, J.; Fernandez, J. R.; Blanco, J.; Carvajal, J. R. Crystallographic study and magnetic structures of CeNi_xPt_{1-x} and diluted related compounds. *Solid State Commun.* **1993**, *87*, 863–868.
- (40) Krikorian, N. The reaction of selected lanthanide carbides with platinum and iridium. *J. Less-Common Met.* **1971**, *23*, 271–279.
- (41) Tsutaoka, T.; Nakamori, Y.; Tokunaga, T.; Itoh, Y. Magnetic and electrical properties of R₇Rh₃ (R= Gd, Tb, Dy, Ho, Er and Y). *J. Phys. Soc. Jpn.* **2001**, *70*, 199–202.
- (42) Moriarty, J.; Humphreys, J.; Gordon, R.; Baenziger, N. X-ray examination of some rare-earth-containing binary alloy systems. *Acta Crystallogr.* **1966**, *21*, 840–841.
- (43) Rehr, J. J.; Kas, J. J.; Vila, F. D.; Prange, M. P.; Jorissen, K. Parameter-free calculations of X-ray spectra with FEFF9. *Phys. Chem. Chem. Phys.* **2010**, *12*, 5503–5513.
- (44) Jones, J.; Xiong, H.; DeLaRiva, A. T.; Peterson, E. J.; Pham, H.; Challa, S. R.; Qi, G.; Oh, S.; Wiebenga, M. H.; Hernández, X. I. P.; et al. Thermally stable single-atom platinum-on-ceria catalysts via atom trapping. *Science* **2016**, *353*, 150–154.
- (45) Ding, K.; Gulec, A.; Johnson, A. M.; Schweitzer, N. M.; Stucky, G. D.; Marks, L. D.; Stair, P. C. Identification of active sites in CO oxidation and water-gas shift over supported Pt catalysts. *Science* **2015**, *350*, 189–192.

- (46) Li, Z.; Xiao, Y.; Chowdhury, P. R.; Wu, Z.; Ma, T.; Chen, J. Z.; Wan, G.; Kim, T.-H.; Jing, D.; He, P.; et al. Direct methane activation by atomically thin platinum nanolayers on two-dimensional metal carbides. *Nat. Catal.* **2021**, *4*, 882–891.
- (47) Sakbodin, M.; Schulman, E.; Cheng, S.; Huang, Y. L.; Pan, Y.; Albertus, P.; Wachsmann, E. D.; Liu, D. Direct Nonoxidative Methane Conversion in an Autothermal Hydrogen-Permeable Membrane Reactor. *Adv. Energy Mater.* **2021**, *11*, No. 2102782.
- (48) Šot, P.; Newton, M. A.; Baabe, D.; Walter, M. D.; van Bavel, A. P.; Horton, A. D.; Copéret, C.; van Bokhoven, J. A. Non-oxidative methane coupling over silica versus silica-supported iron (II) single sites. *Chem. - Eur. J.* **2020**, *26*, 8012–8016.
- (49) Postma, R. S.; Lefferts, L. Influence of axial temperature profiles on Fe/SiO₂ catalyzed non-oxidative coupling of methane. *ChemCatChem* **2020**, *12*, 1–5.
- (50) Jiang, H.; Wang, L.; Cui, W.; Xu, Y. Study on the induction period of methane aromatization over Mo/HZSM-5: partial reduction of Mo species and formation of carbonaceous deposit. *Catal. Lett.* **1999**, *57*, 95–102.
- (51) Kosinov, N.; Uslamin, E. A.; Coumans, F. J.; Wijpkema, A. S.; Rohling, R. Y.; Hensen, E. J. Structure and evolution of confined carbon species during methane dehydroaromatization over Mo/ZSM-5. *ACS Catal.* **2018**, *8*, 8459–8467.
- (52) Vollmer, I.; van der Linden, B.; Ould-Chikh, S.; Aguilar-Tapia, A.; Yarulina, I.; Abou-Hamad, E.; Sneider, Y. G.; Suarez, A. I. O.; Hazemann, J.-L.; Kapteijn, F.; Gascon, J. On the dynamic nature of Mo sites for methane dehydroaromatization. *Chem. Sci.* **2018**, *9*, 4801–4807.
- (53) Kosinov, N.; Wijpkema, A. S.; Uslamin, E.; Rohling, R.; Coumans, F. J.; Mezari, B.; Parastaev, A.; Poryvaev, A. S.; Fedin, M. V.; Pidko, E. A.; Hensen, E. J. M. Confined carbon mediating dehydroaromatization of methane over Mo/ZSM-5. *Angew. Chem., Int. Ed.* **2018**, *57*, 1016–1020.
- (54) Gänzler, A. M.; Casapu, M.; Maurer, F.; Störmer, H.; Gerthsen, D.; Ferré, G.; Vernoux, P.; Bornmann, B.; Frahm, R.; Murzin, V.; et al. Tuning the Pt/CeO₂ interface by in situ variation of the Pt particle size. *ACS Catal.* **2018**, *8*, 4800–4811.
- (55) Zhou, Z.; Guo, H.; Qi, F. Recent developments in synchrotron vacuum ultraviolet photoionization coupled to mass spectrometry. *TrAC, Trends Anal. Chem.* **2011**, *30*, 1400–1409.
- (56) Puente-Urbina, A.; Pan, Z.; Paunović, V.; Šot, P.; Hemberger, P.; van Bokhoven, J. A. Direct Evidence on the Mechanism of Methane Conversion under Non-oxidative Conditions over Iron-modified Silica: The Role of Propargyl Radicals Unveiled. *Angew. Chem., Int. Ed.* **2021**, *60*, 24002–24007.
- (57) Luo, L.; Tang, X.; Wang, W.; Wang, Y.; Sun, S.; Qi, F.; Huang, W.; et al. Methyl radicals in oxidative coupling of methane directly confirmed by synchrotron VUV photoionization mass spectroscopy. *Sci. Rep.* **2013**, *3*, No. 1625.
- (58) Zhang, X.; You, R.; Wei, Z.; Jiang, X.; Yang, J.; Pan, Y.; Wu, P.; Jia, Q.; Bao, Z.; Bai, L.; et al. Radical chemistry and reaction mechanisms of propane oxidative dehydrogenation over hexagonal boron nitride catalysts. *Angew. Chem., Int. Ed.* **2020**, *59*, 8042–8046.
- (59) Bruix, A.; Lykhach, Y.; Matolínová, I.; Neitzel, A.; Skála, T.; Tsud, N.; Vorokhta, M.; Stetsovych, V.; Ševčíková, K.; Mysliveček, J.; et al. Maximum noble-metal efficiency in catalytic materials: atomically dispersed surface platinum. *Angew. Chem., Int. Ed.* **2014**, *53*, 10525–10530.
- (60) Li, X.; Wang, X.; Sadykov, I. I.; Palagin, D.; Safonova, O. V.; Li, J.; Beck, A.; Krumeich, F.; Van Bokhoven, J. A.; Artiglia, L. Temperature and Reaction Environment Influence the Nature of Platinum Species Supported on Ceria. *ACS Catal.* **2021**, *11*, 13041–13049.
- (61) González, I.; Navarro, R.; Wen, W.; Marinkovic, N.; Rodriguez, J.; Rosa, F.; Fierro, J. A comparative study of the water gas shift reaction over platinum catalysts supported on CeO₂, TiO₂ and Ce-modified TiO₂. *Catal. Today* **2010**, *149*, 372–379.
- (62) Steiner, C.; Gänzler, A.; Zehentbauer, M.; Hagen, G.; Casapu, M.; Müller, S.; Grunwaldt, J.-D.; Moos, R. Oxidation state and dielectric properties of ceria-based catalysts by complementary microwave cavity perturbation and X-ray absorption spectroscopy measurements. *Top. Catal.* **2019**, *62*, 227–236.
- (63) Artiglia, L.; Orlando, F.; Roy, K.; Kopelent, R.; Safonova, O.; Nachtegaal, M.; Huthwelker, T.; van Bokhoven, J. A. Introducing time resolution to detect Ce³⁺ catalytically active sites at the Pt/CeO₂ interface through ambient pressure X-ray photoelectron spectroscopy. *J. Phys. Chem. Lett.* **2017**, *8*, 102–108.
- (64) Penner, S.; Wang, D.; Su, D. S.; Rupprechter, G.; Podloucky, R.; Schlögl, R.; Hayek, K. Platinum nanocrystals supported by silica, alumina and ceria: metal–support interaction due to high-temperature reduction in hydrogen. *Surf. Sci.* **2003**, *532–535*, 276–280.
- (65) Chen, J. Z.; Talpade, A.; Canning, G. A.; Probus, P. R.; Ribeiro, F. H.; Datye, A. K.; Miller, J. T. Strong metal-support interaction (SMSI) of Pt/CeO₂ and its effect on propane dehydrogenation. *Catal. Today* **2021**, *371*, 4–10.
- (66) De Graaf, J.; Van Dillen, A.; De Jong, K.; Koningsberger, D. Preparation of highly dispersed Pt particles in zeolite Y with a narrow particle size distribution: characterization by hydrogen chemisorption, TEM, EXAFS spectroscopy, and particle modeling. *J. Catal.* **2001**, *203*, 307–321.
- (67) Puig-Molina, A.; Cano, F. M.; Janssens, T. V. The Cu promoter in an iron–chromium–oxide based water–gas shift catalyst under industrial conditions studied by in-situ XAFS. *J. Phys. Chem. C* **2010**, *114*, 15410–15416.
- (68) Avakyan, L. A.; Kolpacheva, N. A.; Paramonova, E. V.; Singh, J.; Hartfelder, U.; van Bokhoven, J. A.; Bugaev, L. A. Evolution of the atomic structure of ceria-supported platinum nanocatalysts: formation of single layer platinum oxide and Pt–O–Ce and Pt–Ce linkages. *J. Phys. Chem. C* **2016**, *120*, 28057–28066.



JACS Au
AN OPEN ACCESS JOURNAL OF THE AMERICAN CHEMICAL SOCIETY

Editor-in-Chief
Prof. Christopher W. Jones
Georgia Institute of Technology, USA

Open for Submissions 

pubs.acs.org/jacsau  ACS Publications
Most Trusted. Most Cited. Most Read.